



# Atomic and electronic structures of graphene-decorated graphitic carbon nitride ( $g\text{-C}_3\text{N}_4$ ) as a metal-free photocatalyst under visible-light



Taehwan Jeong<sup>a,1</sup>, Huiyan Piao<sup>b,1</sup>, Sangwoo Park<sup>a</sup>, Jae-Hun Yang<sup>h</sup>, Goeun Choi<sup>b</sup>, Qinke Wu<sup>a</sup>, Hyunmin Kang<sup>a</sup>, Hwi Je Woo<sup>a</sup>, Seong Jun Jung<sup>a</sup>, Hanchul Kim<sup>c</sup>, Bong Gyu Shin<sup>d</sup>, Youngkuk Kim<sup>e,f</sup>, Euy Heon Hwang<sup>a,e,g</sup>, Jin-Ho Choy<sup>b,\*\*\*</sup>, Young Jae Song<sup>a,e,f,g,\*</sup>

<sup>a</sup> SKKU Advanced Institute of Nanotechnology (SAINT), Sungkyunkwan University (SKKU), Suwon, 16419, Republic of Korea

<sup>b</sup> Center for Intelligent Nano-Bio Materials (CINBM), Department of Chemistry and Nano Science, Ewha Womans University, Seoul 03760, Republic of Korea

<sup>c</sup> Department of Applied Physics, Sookmyung Women's University, Seoul 140-742, Republic of Korea

<sup>d</sup> Center for Quantum Nanoscience, Institute for Basic Science (IBS), Ewha Womans University, Seoul, 03760, Republic of Korea

<sup>e</sup> Department of Physics, Sungkyunkwan University (SKKU), Suwon, 16419, Republic of Korea

<sup>f</sup> Center for Integrated Nanostructure Physics, Institute for Basic Science (IBS), Sungkyunkwan University (SKKU), Suwon, 16419, Republic of Korea

<sup>g</sup> Department of Nano Engineering, Sungkyunkwan University (SKKU), Suwon, 16419, Republic of Korea

<sup>h</sup> Global Innovative Center for Advanced Nanomaterials, The University of Newcastle, Callaghan, New South Wales, 2308, Australia

## ARTICLE INFO

### Keywords:

Graphitic carbon nitride  
Graphene  
Scanning tunneling spectroscopy  
Hydrogen evolution reaction  
Oxygen evolution reaction

## ABSTRACT

Industrial demands for sustainable and renewable energy resources have inspired studies on photonic and electronic properties of graphitic-carbon nitride ( $g\text{-C}_3\text{N}_4$ ) as a promising photocatalyst without precious metal. The absorption and the yield by metal-free pristine  $g\text{-C}_3\text{N}_4$  are, however, still limited with hydrogen/oxygen evolution reaction (HER/OER) mostly around ultraviolet-light. Here, we propose the graphene-decorated  $g\text{-C}_3\text{N}_4$  as a metal-free photocatalyst under visible-light, based on our atomic-scale measurements and calculations. The  $g\text{-C}_3\text{N}_4$  nanosheets on highly-oriented pyrolytic graphite (HOPG) exhibit band-gaps appropriate for visible-light absorption and work-functions tuned for band alignments to supply electrons and holes for HER/OER. Scanning probe microscopy (SPM) measurements for local density of states (LDOS) in atomic scale and work-functions in nanometer scale with ab initio calculations confirmed the various electronic transitions for each nitrogen and carbon atom in different atomic registries. The graphene-decorated  $g\text{-C}_3\text{N}_4$ , therefore, could provide a breakthrough enabling the efficient water-splitting reactions under visible-light without precious metal.

## 1. Introduction

Hydrogen evolution reaction (HER) by water-splitting has been intensively studied for fuel cells as clean and renewable energy resources [1–11]. However, the applications are hindered by the significantly high cost owing to the inevitable usage of precious metals as catalytic and antioxidant electrodes in electrolysis or photocatalysis, which has inspired extensive studies to reduce the amount of precious metals by mixing catalytic materials such as polymeric carbon nitride (PCN) [12–17]. Among many allotropes of carbon nitrides, graphitic-carbon nitride ( $g\text{-C}_3\text{N}_4$ ) is known to be the most stable phase under ambient conditions [18,19].  $g\text{-C}_3\text{N}_4$  is a graphitic phase of PCN polymerized from triazine or heptazine as a unit molecule. It has been reported that water

can be dissociated by pristine  $g\text{-C}_3\text{N}_4$  nanosheets under ultraviolet light [20]. Although it is challenging, it is required to improve the electronic properties of  $g\text{-C}_3\text{N}_4$  to increase the efficiency of photocatalytic reactions under visible light without precious metals. In this study, we propose a new model system of graphene-decorated  $g\text{-C}_3\text{N}_4$ , which can be applied for the metal-free hydrogen evolution under visible light. We revealed that the graphene-decorated  $g\text{-C}_3\text{N}_4$  has a direct band-gap of 2.51 eV and indirect band-gap of 1.64 eV. The band-gap-engineered electric properties of this metal-free catalyst were confirmed by scanning tunneling microscopy and spectroscopy (STM/STS) and Kelvin probe force microscopy (KPFM) along with density functional theory (DFT) calculations, which explain the electronic structures of the system as a photocatalyst under visible light at the atomic scale.

\* Corresponding author at: SKKU Advanced Institute of Nanotechnology (SAINT), Sungkyunkwan University (SKKU), Suwon, 16419, Republic of Korea.

\*\* Corresponding author.

E-mail addresses: [jhchoy@ewha.ac.kr](mailto:jhchoy@ewha.ac.kr) (J.-H. Choy), [yjsong@skku.edu](mailto:yjsong@skku.edu) (Y.J. Song).

<sup>1</sup> TJ and HP contributed to this work equally.

## 2. Experimental

### 2.1. Preparation of $g\text{-C}_3\text{N}_4$ nanosheets

The cyanamide,  $\text{CH}_2\text{N}_2$  (0.3 g, Alfa Aesar Chemical Co. Ltd. Korea) as a precursor for  $g\text{-C}_3\text{N}_4$  was immobilized in the interlayer space of expandable synthetic clay with chemical formula  $\text{Na}_{0.7}\text{Mg}_{2.65}\text{Si}_4\text{O}_{10}\text{F}_2$  (1 g, CO-OP Chemical Co. Ltd. Japan) under a reaction condition of 100 °C for 3 h, and then thus prepared cyanamid-clay hybrid derivative was further heated up to 550 °C to realize the formation of  $g\text{-C}_3\text{N}_4$  in the 2D clay lattice. Finally, the nanosheet  $g\text{-C}_3\text{N}_4$  was separated out from  $g\text{-C}_3\text{N}_4$ -clay hybrid simply by dissolving clay only in hydrofluoric acid at 0 °C for 4 h. The fluorinated impurity possibly on nanosheet  $g\text{-C}_3\text{N}_4$  was also removed by hydrochloric acid at 80 °C for 1 h. Thus, obtained suspension was washed with deionized water to remove the residual acid. The bulk  $g\text{-C}_3\text{N}_4$ , as a control, was also prepared by heating the cyanamide at 550 °C for 4 h with the heating rate of 3 °C/min [21].

### 2.2. Characterization of $g\text{-C}_3\text{N}_4$ nanosheets

The X-ray diffraction (XRD) patterns for the samples were recorded with a Rigaku RINT-Ultima III diffractometer using Ni-filtered  $\text{Cu-K}\alpha$  radiation ( $\lambda = 1.5405 \text{ \AA}$ ) operated at 40 kV and 30 mA. The diffuse reflectance UV-vis spectra were measured with Jasco V-550 spectrophotometer equipped with an integrating sphere by using  $\text{BaSO}_4$  plate as a baseline. Fourier transform infrared (FT-IR) spectra were obtained from Jasco FT/IR 6100 spectrophotometer by using KBr pellet method. Electron energy loss spectroscopy (EELS) analyses were performed using a JEM ARM-200 F microscope equipped with an EELS detector (965 GIF Quantum ER, GATAN, US) at 80 kV. According to XRD analyses for the bulk  $g\text{-C}_3\text{N}_4$  and  $g\text{-C}_3\text{N}_4$  nanosheets as shown in Figure S1(a), the peak at 27.5° corresponding to the (002) plan was observed in both cases, though the peak intensity for the latter was significantly reduced due to the fact that the  $g\text{-C}_3\text{N}_4$  nanosheets were restacked with a limited degree with the thickness of ~ 4.2 nm. To explore the difference in molecular structure of the  $g\text{-C}_3\text{N}_4$  nanosheets compared to the bulk  $g\text{-C}_3\text{N}_4$ , FT-IR spectroscopic studies were performed as shown in Figure S1(b) and Table S1. The overall spectral feature for both samples were turned out to be the same except a peak at  $2170 \text{ cm}^{-1}$ , which can be attributed to cyano terminal groups such as  $\text{C}\equiv\text{N}$  and  $\text{N} = \text{C}=\text{N}$ , probably due to the formation of small fragment of diazo groups on the surface of  $g\text{-C}_3\text{N}_4$  nanosheets [22,23]. The absorption edge of  $g\text{-C}_3\text{N}_4$  nanosheets in UV-vis DRS (Figure S3(c)) exhibited a remarkable blue shift from 455 to 430 nm compared to the bulk  $g\text{-C}_3\text{N}_4$ , surely due to the quantum size effect. As shown in EELS analysis (Figure S3(d)), the bonding nature of  $g\text{-C}_3\text{N}_4$  nanosheets was determined to be the  $\text{sp}^2$  type, as can be seen from the strong  $\pi^*$  peaks at C K-edge and N-K-edge, respectively [24]. The atomic ratios of N/C from the EELS analysis for the  $g\text{-C}_3\text{N}_4$  nanosheets and the bulk  $g\text{-C}_3\text{N}_4$  were calculated to be 1.31 and 1.32, respectively, which were in good agreement with the theoretical one of 1.33.

Preparation of  $g\text{-C}_3\text{N}_4$  on HOPG: The  $g\text{-C}_3\text{N}_4$  nanosheets were dispersed in ethanol, and this colloidal was sprayed on highly oriented pyrolytic graphite (HOPG) by mist-spraying followed by a spin-coater (1 min, 1000 rpm). This sample was annealed at ~500 °C for 24 h in the UHV chamber before loaded into the STM head.

### 2.3. Measurements of STM and STS

Preparation chamber was used to clean ex-situ sample, the base pressure less than  $5 \times 10^{-10}$  torr. Besocke type home-built STM was used to measure STM and STS, the base pressure less than  $1 \times 10^{-10}$  torr. It operated at room temperature and 50 mV at 931 Hz lock-in modulation signal was used for tunneling spectroscopy. A chemically-etched W tip was annealed with an e-beam before use.

### 2.4. DFT calculations

We performed first-principles calculations based on DFT as implemented in the Vienna ab initio Simulation Package (VASP) [25–28]. We used the Perdew–Burke–Ernzerhof exchange–correlation functional with the projector augmented wave pseudopotentials provided by VASP [29]. All DFT calculations in this work include the van der Waals correction base on the semiempirical form of DFT-D2, suggested by Grimme et al. [30]. The cut-off energy for the plane-wave basis was set as 500 eV and the convergence criterion of atomic force for geometric optimization was set at 0.01 eV/Å. The vacuum region was set as 20 Å to eliminate interactions between periodic boundaries. A Monkhorst pack [31]  $4 \times 4 \times 1$  k-point mesh was used for the optimization of the structures and the  $32 \times 32 \times 1$  k-point mesh was used for the calculation of DOS.

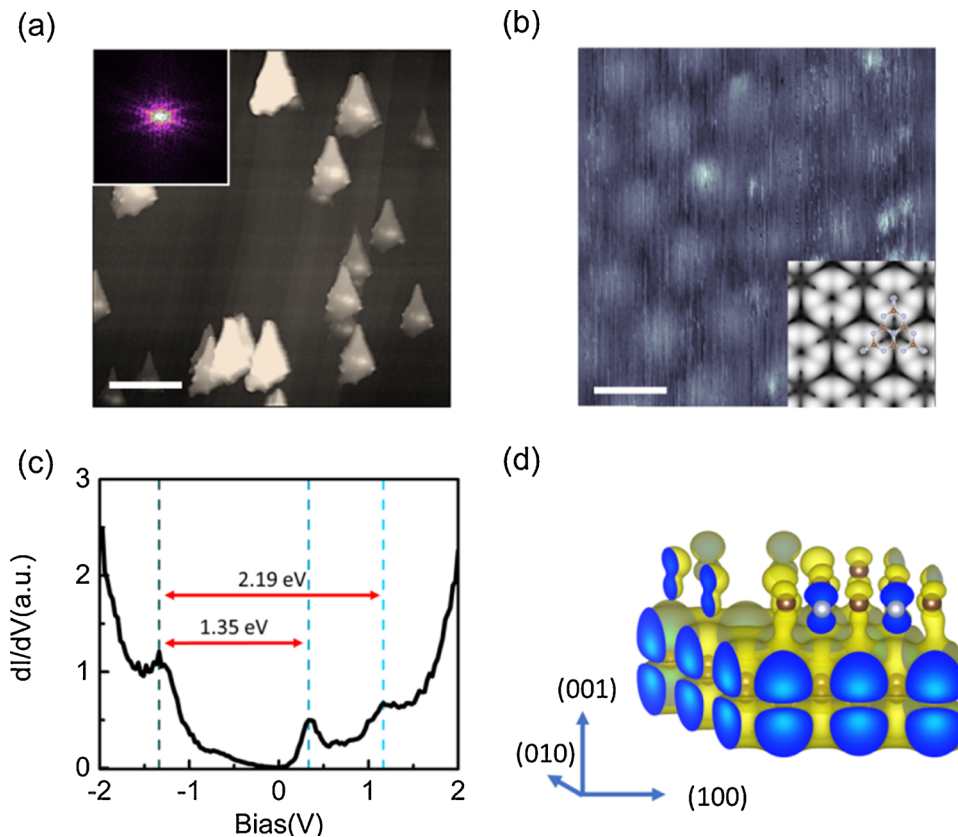
### 2.5. Measurements of KPFM

We operated a commercial atomic force microscope (AFM), *i.e.* a NX10 Model (Park Systems Co.) for topographic and surface potential measurements. A non-contact electric force microscopy (EFM) mode in NX10 was used for Kelvin probe force microscopy (KPFM) measurements with NSC36/Cr-Au tips (MikroMasch Co.) and conductive sample holders for an electrical ground to the samples.

## 3. Results and discussion

The  $g\text{-C}_3\text{N}_4$ /graphene heterostructure is composed of chemically inert and mechanically robust materials; an efficient HER with  $g\text{-C}_3\text{N}_4$ /graphene was already reported [32,33]. The model system of  $g\text{-C}_3\text{N}_4$ /graphene in this study was prepared by depositing  $g\text{-C}_3\text{N}_4$  nanosheets on a highly oriented pyrolytic graphite (HOPG) substrate, as described in Methods, Figure S1 and table S1. Although HOPG is a bulk phase, the top layer is floating a bit more with broken symmetry in the c-axis. We measured linear dispersion relation between energy and density of states at the low bias regime in Figure S2. **Fig. 1(a)** shows an atomic force microscopy (AFM) image; the inset shows the corresponding fast-Fourier-transform (FFT) data. The results imply that all of the  $g\text{-C}_3\text{N}_4$  nanosheets with different thicknesses are epitaxially deposited on HOPG. **Fig. 1(b)** shows a high-resolution STM image which was measured on thick  $g\text{-C}_3\text{N}_4$  flakes. The inset is a DFT-simulated image with the ball-stick model of  $g\text{-C}_3\text{N}_4$ , which shows a good agreement with the measurements. **Fig. 1(c)** is the STS data showing the change of the electronic structure in the graphene decorated  $g\text{-C}_3\text{N}_4$  system, and **Fig. 1(d)** is a three-dimensional plot of the charge distribution for visualizing the overlapped orbital between graphene and  $g\text{-C}_3\text{N}_4$ . The energy range is -0.4 eV to -0.2 eV under  $5.0 \times 10^{-6}$  (electrons /  $\text{\AA}^3$ ).

Among the large number of reported PCNs, mostly aimed for photoelectronic applications,  $g\text{-C}_3\text{N}_4$  is considered the most promising material for photocatalysts. A previous study predicted that the heptazine-based  $g\text{-C}_3\text{N}_4$  has two different stable configurations, as shown in **Fig. 2(a)** and (b) [34]. One of them is a buckled configuration, shown in **Fig. 2(a)**, while the other is a planar configuration, shown in **Fig. 2(b)**. A negligible difference in crystallography is observed between the buckled and planar phases (only a small mismatch of the lattice constant by 0.2 Å due to buckling), while their electronic structures are distinguishable from each other. The buckled phase has only a direct band-gap of 2.87 eV, while the planar phase has both direct and indirect band-gaps of 2.66 eV and 2.27 eV, respectively. We used only the planar phase of  $g\text{-C}_3\text{N}_4$  nanosheets in this study, as confirmed by photoluminescence (PL) and STS measurements. The PL spectrum in **Fig. 2(c)** shows the optical band-gap at 581 nm (2.13 eV), which is very close to the prediction for the indirect band-gap of the planar phase. Moreover, the local density of states (LDOS) measured by STS in **Fig. 2(d)** shows two distinct band-gaps of 2.20 eV and 2.79 eV, which can be assigned to the indirect and direct band-gaps of the planar phase, respectively.



These spectroscopic data confirm that the  $g\text{-C}_3\text{N}_4$  nanosheets in this study mostly exhibit the planar phase.

Careful STS measurements were performed on the different atomic registries of carbon and nitrogen, *i.e.*, carbon (C), nitrogen at the edge

( $\text{N}_E$ ), nitrogen at the center ( $\text{N}_C$ ), and nitrogen at the bridge ( $\text{N}_B$ ), to investigate the electronic structures of  $g\text{-C}_3\text{N}_4$ /graphene heterostructures and understand the origin of HER. The band edges need to be considered to discuss about the absorption band for the external light

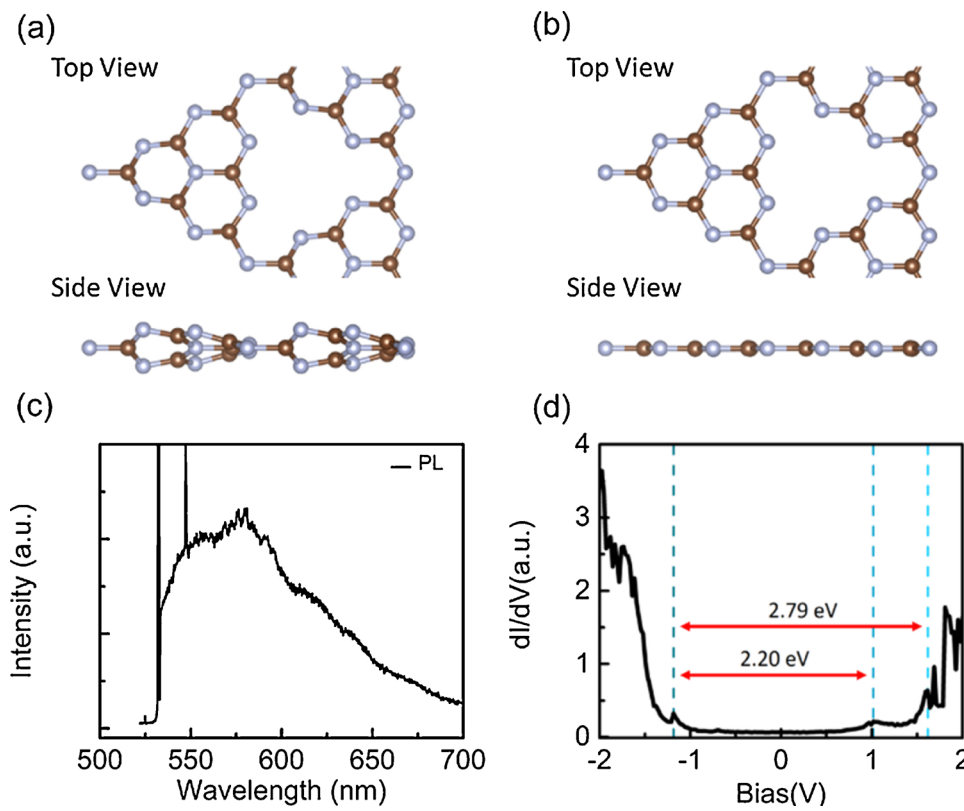


**Fig. 2.** Phases and electronic structures of the pristine  $g\text{-C}_3\text{N}_4$  used in this study. Ball-stick models of the (a) buckled and (b) planar phases of  $g\text{-C}_3\text{N}_4$  with top and side views. Carbon and nitrogen atoms are shown in brown and light blue, respectively. (c) PL data of  $g\text{-C}_3\text{N}_4$  nanosheets on  $\text{SiO}_2$  with sharp peaks from the substrate. (d) STS data measured on a thick  $g\text{-C}_3\text{N}_4$  flake with a thickness of 4.2 nm; the indirect and direct band-gaps are indicated. This spectrum was measured with a set-point current of 0.5 nA and lock-in modulation of 50 mV at 931 Hz, at room temperature (For interpretation of the references to colour in this figure legend, the reader is referred to the web version of this article).

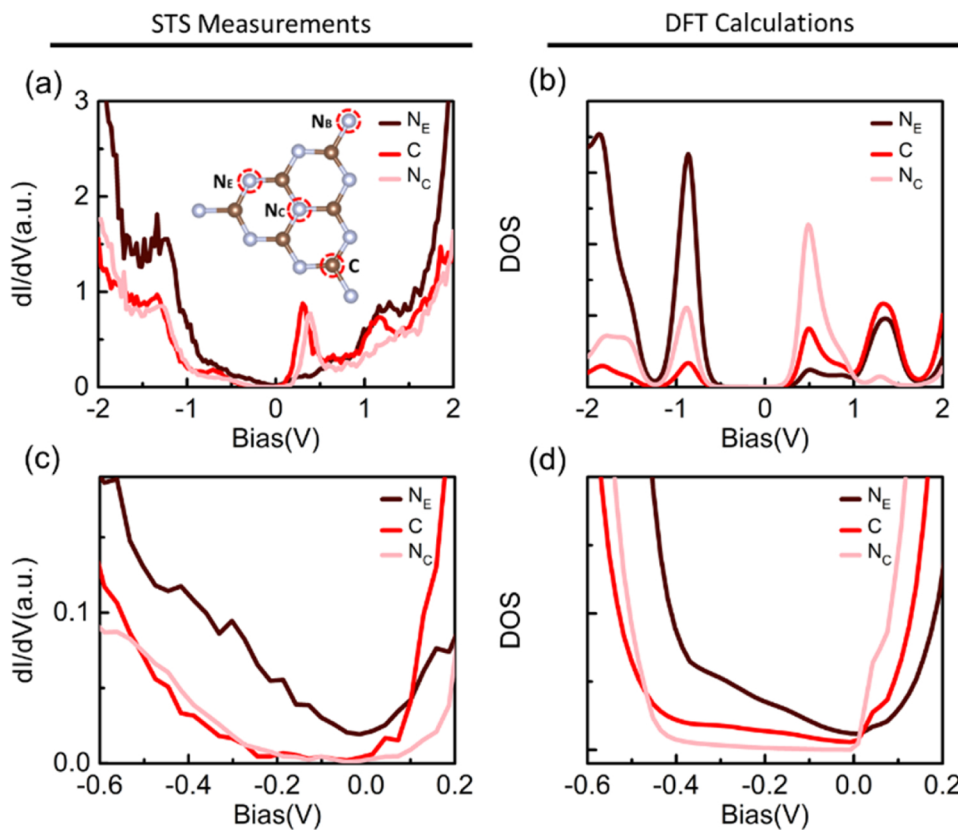


**Fig. 3.** Figure Caption Measured and calculated electronic structures of  $g\text{-C}_3\text{N}_4$  at the atomic scale. (a) STS measured on different atomic registries of  $g\text{-C}_3\text{N}_4$  on HOPG. The inset identifies carbon (C), nitrogen at the edge ( $N_E$ ), nitrogen at the center ( $N_C$ ), and nitrogen at the bridge ( $N_B$ ). (b) DFT calculations for the atomic registries of  $g\text{-C}_3\text{N}_4$  on HOPG, which show good agreement with Fig. 3(a). (c) and (d) Magnified views of the measured and calculated spectra in Fig. 3(a) and (b) near the Fermi level, respectively. These STS results were measured with a set-point current of 0.5 nA and lock-in modulation of 50 mV at 931 Hz, at room temperature.

[35–41], but the peak position has been analyzed in this work by STS measurements in an atomic scale with DFT calculations to explain shrinking the band-gap with an appropriate workfunction of graphene-decorated  $g\text{-C}_3\text{N}_4$  for HER applications in a visible light regime.

The inset in Fig. 3(a) illustrates the different atomic registries. Fig. 3(a) shows STS spectra measured on C,  $N_E$ , and  $N_C$ , while Fig. 3(b) shows the corresponding DFT calculations for each atomic registry, which are in good agreement with each other. The calculations were performed in three different atomic configurations Figure S4 (a)–(c) included the lowest-energy atomic configuration [42]. For conveniences, we named “nitrogen-AB stacking” for (a), “carbon-AB stacking” for (b) and “AA stacking” for (c). However, we didn’t compare all cases due to differences of DOS near the fermi level. We focused on nitrogen-AB stacking system, the reason will discuss in next paragraph. Compared with the LDOS of the bulk phase in Fig. 2(d), the graphene-decorated  $g\text{-C}_3\text{N}_4$  exhibits different electronic structures with a narrower band-gap than that of the bulk  $g\text{-C}_3\text{N}_4$ . As illustrated in the inset of Fig. 3(a), all of the carbon atoms have the same local environment, leading to a symmetric bonding with the three nearest-neighbor nitrogen atoms. Similarly,  $N_C$  and  $N_B$  sites are equivalent, considering only the chemical bonding with the nearest-neighbor carbon atoms of  $g\text{-C}_3\text{N}_4$ . Indeed, we confirmed that these two nitrogen atoms have the same DOS by both experimental measurements and DFT calculations. Therefore, in Fig. 3(a) and (b), we present only the spectrum for  $N_C$ . Unlike  $N_C$  or  $N_B$ ,  $N_E$  has two additional unpaired electrons, leading to a different LDOS from those of  $N_C$  and  $N_B$ . The STS in Fig. 3(a) shows three characteristic peaks at approximately -1.34, +0.30, and +1.17 eV, which correspond to -0.86, +0.49, and 1.33 eV in the calculated LDOS in Fig. 3(b), respectively. Compared with the band structure in Figure S5, the peaks around -0.86 eV in Fig. 3(b) can be assigned to the valence band edge at the point. A Dirac point of graphene exists at the point owing to the 33 supercell for hybrid structure calculations. [43] The band-gap between the peaks at -0.86 eV and +0.49 eV corresponds to the indirect band-gap from the (0 0 0) point to

the Y(-0.5 0 0.5) and T(-0.5 0.5 0.5) points. On the other hand, the band-gap between -0.86 eV and +1.33 eV corresponds to the direct band-gap at the point. From these observations, we expect that the excited electrons at  $N_E$  should undergo a direct band transition, considering the negligible states at the S point, while the electrons at  $N_C$  (as well as  $N_B$ ) should significantly contribute to an indirect band transition from -0.86 eV to +0.49 eV. Moreover, the excited electrons at  $N_E$  can undergo an indirect band transition to the S point of the neighboring carbon atoms of  $g\text{-C}_3\text{N}_4$ . The large number of electrons near  $N_E$  can be excited through a direct band-gap of 2.19 eV or indirect band-gap of 1.35 eV by hopping to the nearest-neighbor carbon atoms of  $g\text{-C}_3\text{N}_4$ . This explains the mechanism at the atomic scale that the band-gap of the  $g\text{-C}_3\text{N}_4$  nanosheets on the HOPG is tuned to the value corresponding to the visible-light regime. Unlike the general tendency of two-dimensional materials that their band-gaps decrease with the increase in their thicknesses, the decoration of graphene to thin  $g\text{-C}_3\text{N}_4$  nanosheets yielded the reduced band-gap. Fig. 3(c) and (d) shows magnified LDOS of Fig. 3(a) and (b), respectively, which agree well with each other. We attribute this seemingly counter-intuitive result to the strong coupling between  $g\text{-C}_3\text{N}_4$  and graphene. As the thickness of  $g\text{-C}_3\text{N}_4$  is sufficiently small for tunneling, we were able to observe weak signatures of a Dirac cone of the underlying graphene in both measured and calculated LDOSs. Even though this signature of graphene is significantly weaker than the resonance energy peaks of  $g\text{-C}_3\text{N}_4$ , it is sufficiently discernible to show that the energy locations of Dirac points vary depending on the atomic sites. This implies that charge imbalance exists at the graphene/ $g\text{-C}_3\text{N}_4$  interface due to the strong coupling depending on the atomic registry which may induce the enhancement of dielectric function by calculations as reported previously [44]. We consider that the shift of Dirac cones is an evidence of the strong coupling between  $g\text{-C}_3\text{N}_4$  and graphene, responsible for the reduction in the band-gap.

Further investigations were performed by KPFM measurements to elucidate the energy locations of the conduction and valence band edges, which are of crucial importance for HER and OER applications.

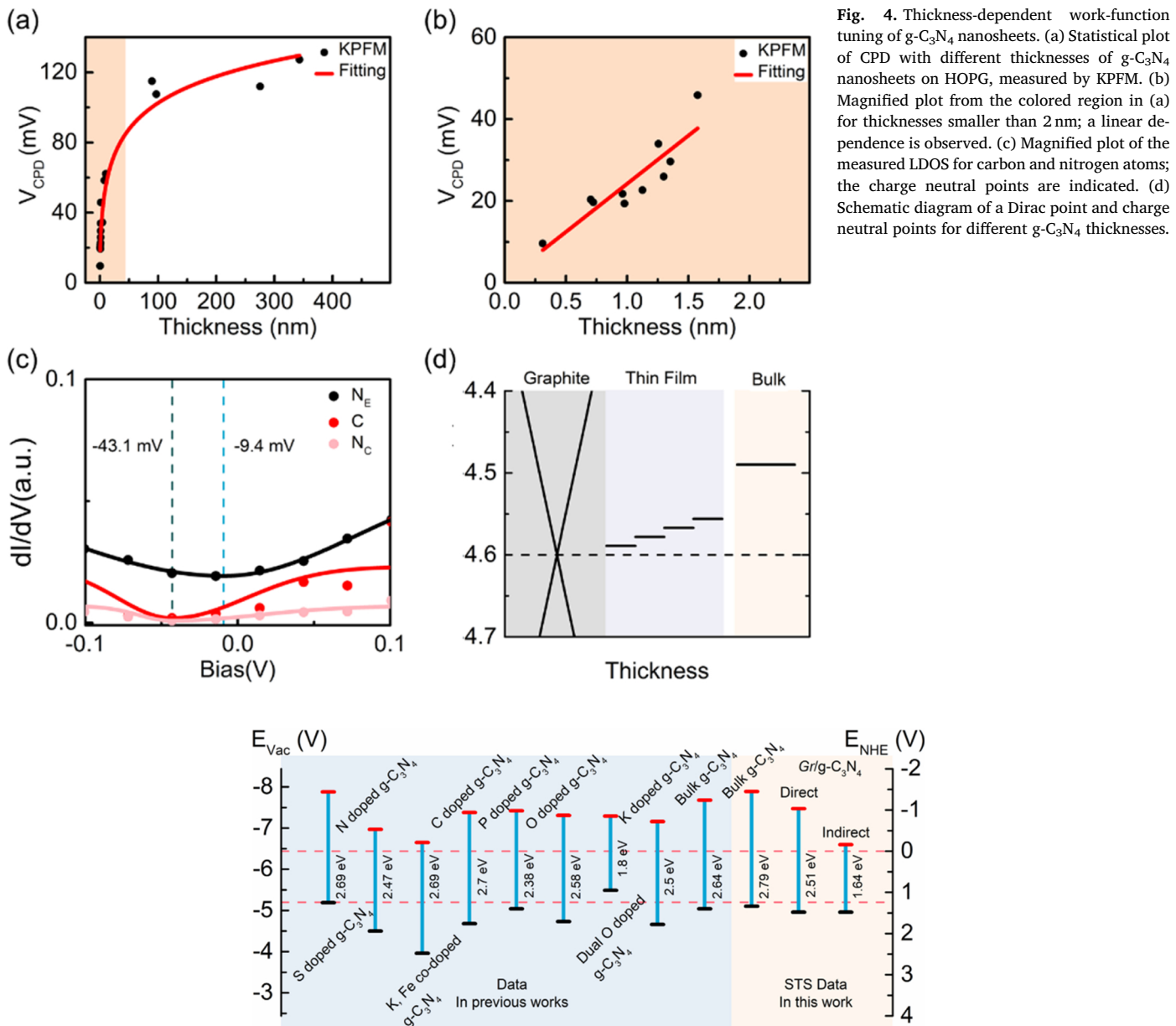


**Fig. 5.** Figure Caption Energy level diagram for various photocatalysts. The energy level diagrams of doped g-C<sub>3</sub>N<sub>4</sub> [45–52] series were reported in previous studies. The measured values of various g-C<sub>3</sub>N<sub>4</sub> structures are plotted for the bulk phase; the direct and indirect band-gaps of the graphene-decorated system are shown.

The spatial mapping of the thickness-dependent surface potential by KPFM, as well as atom-dependent LDOS measurements by STS, can reveal the energy alignments of g-C<sub>3</sub>N<sub>4</sub>/graphene heterostructures. Fig. 4(a) shows a statistical plot of contact potential difference (CPD) of KPFM measurements for different g-C<sub>3</sub>N<sub>4</sub> thicknesses on HOPG, which is a good substrate for the estimation of potential difference considering its work-function of 4.6 eV. As shown in Fig. 4(b) which presents a magnified view of Fig. 4(a), while the bulk-phase g-C<sub>3</sub>N<sub>4</sub> saturates to 120 mV, thin g-C<sub>3</sub>N<sub>4</sub> nanosheets on HOPG exhibit a linear dependence of the CPD for thicknesses smaller than 2 nm with a value of 11 mV for monolayer g-C<sub>3</sub>N<sub>4</sub>. As partly explained in Fig. 3, the work-function change of the graphene-decorated g-C<sub>3</sub>N<sub>4</sub> can be understood at the atomic scale. Fig. 4(c) further magnifies the spectra of Fig. 3(c) in the sample bias range of -100 mV to +100 mV. Although both N<sub>E</sub> and N<sub>C</sub> are located on top of hollow sites of the underlying graphene, they have different charge neutral points of -9.4 mV for N<sub>E</sub> and -43.1 mV for N<sub>C</sub>, which implies a strong atomic-registry-dependent interaction between g-C<sub>3</sub>N<sub>4</sub> and graphene, as mentioned above.

This occurs as N<sub>E</sub> is electron-rich, unlike N<sub>C</sub>, owing to an extra pair of electrons that do not participate in atomic bonding. The shift of the charge neutral point by 9.4 mV from the Fermi level in Fig. 4(c) is very similar to the value of CPD in Fig. 4(b). As the surface potential is determined by electrons on the surface, the six N<sub>E</sub> sites in the unit cell dominate the surface potential of the g-C<sub>3</sub>N<sub>4</sub>/graphene heterostructures. The energy locations of charge neutral points on C and N<sub>C</sub> are shifted further away from the Fermi level owing to the in-plane electric field induced by the charge distribution of g-C<sub>3</sub>N<sub>4</sub>. We can see this energy shift not only Fig. 4(d) but also Figure S4(d)–(f). When compared with Figure S4(e) and (f), the energy structures of carbon of g-C<sub>3</sub>N<sub>4</sub> and N<sub>C</sub> are shifted by 200 mV, and N<sub>E</sub> is shifted by 100 mV. These energy shifts are originated from the distortion of g-C<sub>3</sub>N<sub>4</sub> while the nitrogen atoms at the edge (N<sub>E</sub>) on hollow sites of graphene in our nitrogen-AB stacking configuration can maintain g-C<sub>3</sub>N<sub>4</sub> in a planar phase in (d). Therefore, the work-function location could be understood by comparing the STS at the atomic scale and thickness-dependent KPFM data summarized in Fig. 4(d).

Fig. 5 presents an energy diagram showing the conduction and valence bands for well-known photocatalytic materials, including our measurements of g-C<sub>3</sub>N<sub>4</sub>/graphene with the corresponding band-gaps. The left ordinate represents the energy from the vacuum level, while the right ordinate represents the normal hydrogen electrode (N<sub>CE</sub>) at pH = 0. The two horizontal dashed lines represent the energies for HER and OER. As summarized in this Figure, the metal-free photocatalyst of g-C<sub>3</sub>N<sub>4</sub>/graphene heterostructures can have band-gaps appropriate for visible-light applications and band alignments for HER and OER. The comparison with the other materials in this plot and other precious photocatalytic metals reveals that the g-C<sub>3</sub>N<sub>4</sub>/graphene heterostructure is a promising photocatalyst candidate for visible-light applications.

#### 4. Conclusion

In the process which improvement of efficient precious metal free photocatalyst [35–41,45–54], the g-C<sub>3</sub>N<sub>4</sub> epitaxially decorated with graphene was proposed as a photocatalyst for HER and OER applications. This heterostructure had a direct band-gap of 2.51 eV and indirect band-gap of 1.64 eV, representing the best fit to visible light. The band structures were obtained by STS measurements at the atomic scale, supported by DFT calculations. Band alignments appropriate for HER and OER could be confirmed by thickness-dependent CPD measurements by KPFM and atomic registry-dependent spectra by STS. Nitrogen atoms at the edge (N<sub>E</sub>) were crucial to tune the surface potential associated with their extra pair of electrons with a direct band-gap. Moreover, N<sub>E</sub> supported electronic transitions through an indirect band-gap to neighboring carbon atoms, while the other nitrogen and carbon atoms had indirect band-gaps. Therefore, the graphene-decorated g-C<sub>3</sub>N<sub>4</sub> is a promising, efficient, metal-free, chemically stable, and mechanically robust photocatalyst for HER and OER in water-splitting under visible light.

#### Acknowledgements

This research was supported by Institute for Basic Science Grant Nos. IBS-R011-D1 and IBS-R027-D1), the Basic Science Research Program Grant No. 2015M3A7B4050455, the SRC Center for Topological Matter Grant No. 2018R1A5A6075964, the Pioneer Research Center Program Grant No. NRF-2014M3C1A3053029, and through the National Research Foundation (NRF) funded by the Ministry of Science, ICT & Future Planning (MSIP), Korea. This research was also supported by Construction Technology Research Project Grant No. 18SCIP-B146646-01 funded by the Ministry of Land, Infrastructure and Transport in Korea, and by Industrial Strategic Technology Development Program Grant No. 10085617 funded by the Ministry of Trade Industry & Energy (MOTIE) in Korea. Supercomputing resources including technical service were supported by National Institute of Supercomputing and Network through Korea Institute of Science and Technology Information KSC-2018-S1-0008.

#### Appendix A. Supplementary data

Supplementary material related to this article can be found, in the online version, at doi:<https://doi.org/10.1016/j.apcatb.2019.117850>.

#### References

- [1] J. Yu, J. Jin, B. Cheng, M. Jaroniec, A noble metal-free reduced graphene oxide–CdS nanorod composite for the enhanced visible-light photocatalytic reduction of CO<sub>2</sub> to solar fuel, *J. Mater. Chem. A* 2 (2014) 3407–3416, <https://doi.org/10.1039/C3TA14493C>.
- [2] S. Sun, W. Wang, D. Jiang, L. Zhang, X. Li, Y. Zheng, Q. An, Bi<sub>2</sub>WO<sub>6</sub> quantum dot-intercalated ultrathin montmorillonite nanostructure and its enhanced photocatalytic performance, *Nano Res.* 7 (2014) 1497–1506, <https://doi.org/10.1007/s12274-014-0511-2>.
- [3] K. Maeda, K. Teramura, D. Lu, T. Takata, N. Saito, Y. Inoue, K. Domen, Characterization of Rh–Cr mixed-oxide nanoparticles dispersed on (Ga<sub>1-x</sub>Zn<sub>x</sub>)(N<sub>1-x</sub>Ox) as a cocatalyst for visible-light-driven overall water splitting, *J. Phys. Chem. B* 110 (2006) 13753–13758, <https://doi.org/10.1021/jp061829o>.
- [4] J. Zhu, F. Fan, R. Chen, H. An, Z. Feng and C. Li, Direct imaging of highly anisotropic photogenerated charge separations on different facets of a single BiVO<sub>4</sub> photocatalyst, *Angew. Chem. Int. Ed.* 54 (31) 9111–9114. doi:10.1002/anie.201504135.
- [5] F. Xu, Y. Shen, L. Sun, H. Zeng, Y. Lu, Enhanced photocatalytic activity of hierarchical ZnO nanoplate-nanowire architecture as environmentally safe and facilely recyclable photocatalyst, *Nanoscale* 3 (2011) 5020–5025, <https://doi.org/10.1039/C1NR11033K>.
- [6] A. Kudo, Y. Miseki, Heterogeneous photocatalyst materials for water splitting, *Chem. Soc. Rev.* 38 (2008) 253–278, <https://doi.org/10.1039/B800489G>.
- [7] H. Sakamoto, T. Ohara, N. Yasumoto, Y. Shiraishi, S. Ichikawa, S. Tanaka, T. Hirai, Hot-electron-Induced highly efficient O<sub>2</sub> activation by Pt nanoparticles supported on Ta<sub>2</sub>O<sub>5</sub> driven by visible light, *J. Am. Chem. Soc.* 137 (2015) 9324–9332, <https://doi.org/10.1021/jacs.5b04062>.
- [8] S. Han, L. Hu, Z. Liang, S. Wagel, A.A. Al-Ghamdi, Y. Chen and X. Fang, One-step hydrothermal synthesis of 2D hexagonal nanoplates of  $\alpha$ -Fe<sub>2</sub>O<sub>3</sub>/graphene composites with enhanced photocatalytic activity, *Adv. Funct. Mater.* 24 (36) 5719–5727, <https://doi.org/10.1002/adfm.201401279>.
- [9] A.L. Linsebigler, G. Lu, J.T. Yates Jr, Photocatalysis on TiO<sub>2</sub> surfaces: principles, mechanisms, and selected results, *Chem. Rev.* 95(3) (1995) 735–758, <https://doi.org/10.1021/cr0035a013>.
- [10] K. Domen, S. Naito, M. Soma, T. Onishi, K. Tamaru, Photocatalytic decomposition of water vapour on an NiO–SrTiO<sub>3</sub> catalyst, *J. Chem. Soc. Chem. Commun.* 0 (1980) 543–544, <https://doi.org/10.1039/C39800000543>.
- [11] W.J. Youngblood, S.-H.A. Lee, K. Maeda, T.E. Mallouk, Visible light water splitting using dye-sensitized oxide semiconductors, *Acc. Chem. Res.* 42 (2009) 1966–1973, <https://doi.org/10.1021/ar9002398>.
- [12] K. Schwinghammer, M.B. Mesch, V. Duppel, C. Ziegler, J. Senker, B.V. Lotsch, Crystalline carbon nitride nanosheets for improved visible-light hydrogen evolution, *J. Am. Chem. Soc.* 136 (2014) 1730–1733, <https://doi.org/10.1021/ja411321s>.
- [13] M.J. Bojdys, J.-O. Müller, M. Antonietti and A. Thomas, Ionothermal synthesis of crystalline, condensed, graphitic carbon nitride, *Chem. – Eur. J.* 14 (27) 8177–8182, <https://doi.org/10.1002/chem.200800190>.
- [14] E. Wirnhier, M. Döblinger, D. Gunzelmann, J. Senker, B.V. Lotsch and W. Schnick, Poly(triazine imide) with Intercalation of Lithium and Chloride Ions [(C<sub>3</sub>N<sub>3</sub>)<sub>2</sub>(NH<sub>2</sub>Li<sub>1-x</sub>)<sub>3</sub>·LiCl]: a crystalline 2D carbon nitride network, *Chem. – Eur. J.* 17 (11) 3213–3221, <https://doi.org/10.1002/chem.201002462>.
- [15] M. Döblinger, B.V. Lotsch, J. Wack, J. Thun, J. Senker, W. Schnick, Structure elucidation of polyheptazine imide by electron diffraction—a templated 2D carbon nitride network, *Chem. Commun.* 0 (2009) 1541–1543, <https://doi.org/10.1039/B820032G>.
- [16] G. Algarra-Siller, N. Severin, S.Y. Chong, T. Björkman, R.G. Palgrave, A. Laybourn, M. Antonietti, Y.Z. Khimyak, A.V. Krasheninnikov, J.P. Rabe, U. Kaiser, A.I. Cooper, A. Thomas and M.J. Bojdys, Triazine-based graphitic carbon nitride: a two-dimensional semiconductor, *Angew. Chem. Int. Ed.* 53 (29) 7450–7455. <https://doi.org/10.1002/anie.201402191>.
- [17] B.V. Lotsch, M. Döblinger, J. Sehnert, L. Seyfarth, J. Senker, O. Oeckler and W. Schnick, Unmasking melon by a complementary approach employing electron diffraction, solid-state NMR spectroscopy, and theoretical calculations—structural characterization of a carbon nitride polymer, *Chem. – Eur. J.* 13 (17) 4969–4980, <https://doi.org/10.1002/chem.200601759>.
- [18] A. Thomas, A. Fischer, F. Goettmann, M. Antonietti, J.-O. Müller, R. Schlögl, J. Carlsson, Cheminform abstract: graphitic carbon nitride materials: variation of structure and morphology and their use as metal-free catalysts, *J. Mater. Chem.* v.18, (2008) 4893–4908, <https://doi.org/10.1039/B800274F> 40.
- [19] E. Kroke, M. Schwarz, E. Horath-Bordon, P. Kroll, B. Noll, A.D. Norman, Tri-s-triazine derivatives. Part I. From trichloro-tri-s-triazine to graphitic C 3 N 4 structures, *New J. Chem.* 26 (2002) 508–512, <https://doi.org/10.1039/B111062B>.
- [20] J. Liu, Y. Liu, N. Liu, Y. Han, X. Zhang, H. Huang, Y. Lifshitz, S.-T. Lee, J. Zhong, Z. Kang, Metal-free efficient photocatalyst for stable visible water splitting via a two-electron pathway, *Science* 347 (2015) 970–974, <https://doi.org/10.1126/science.aaa3145>.
- [21] M.J. Bojdys, J.-O. Müller, M. Antonietti, A. Thomas, Ionothermal synthesis of crystalline, condensed, graphitic carbon nitride, *Chemistry* 14 (2008) 8177–8182, <https://doi.org/10.1002/chem.200800190>.
- [22] S. Cao, J. Low, J. Yu, M. Jaroniec, Polymeric photocatalysts based on graphitic carbon nitride, *Adv. Mater. Weinheim* 27 (2015) 2150–2176, <https://doi.org/10.1002/adma.201500033>.
- [23] Y. Yu, Q. Zhou, J. Wang, The ultra-rapid synthesis of 2D graphitic carbon nitride nanosheets via direct microwave heating for field emission, *Chem. Commun.* 52 (2016) 3396–3399, <https://doi.org/10.1039/C5CC10258H>.
- [24] M. Zelisko, Y. Hanlumyuang, S. Yang, Y. Liu, C. Lei, J. Li, P.M. Ajayan, P. Sharma, Anomalous piezoelectricity in two-dimensional graphene nitride nanosheets, *Nat. Commun.* 5 (2014) 4284, <https://doi.org/10.1038/ncomms5284>.
- [25] G. Kresse, J. Hafner, Ab initio molecular dynamics for liquid metals, *Phys. Rev. B* 47 (1993) 558–561, <https://doi.org/10.1103/PhysRevB.47.558>.
- [26] G. Kresse, J. Hafner, Ab initio molecular-dynamics simulation of the liquid-metal-amorphous-semiconductor transition in germanium, *Phys. Rev. B* 49 (1994) 14251–14269, <https://doi.org/10.1103/PhysRevB.49.14251>.
- [27] G. Kresse, J. Furthmüller, Efficiency of ab-initio total energy calculations for metals and semiconductors using a plane-wave basis set, *Comput. Mater. Sci.* 6 (1996) 15–50, [https://doi.org/10.1016/0927-0256\(96\)00008-0](https://doi.org/10.1016/0927-0256(96)00008-0).
- [28] G. Kresse, J. Furthmüller, Efficient iterative schemes for ab initio total-energy

calculations using a plane-wave basis set, *Phys. Rev. B* 54 (1996) 11169–11186, <https://doi.org/10.1103/PhysRevB.54.11169>.

[29] J.P. Perdew, K. Burke, M. Ernzerhof, Generalized gradient approximation made simple, *Phys. Rev. Lett.* 77 (1996) 3865–3868, <https://doi.org/10.1103/PhysRevLett.77.3865>.

[30] S. Grimme, Semiempirical GGA-type density functional constructed with a long-range dispersion correction, *J. Comput. Chem.* 27(15), 1787–1799. <https://doi.org/10.1002/jcc.20495>.

[31] H.J. Monkhorst, J.D. Pack, Special points for Brillouin-zone integrations, *Phys. Rev. B* 13 (1976) 5188–5192, <https://doi.org/10.1103/PhysRevB.13.5188>.

[32] K. Chen, Z. Chai, C. Li, L. Shi, M. Liu, Q. Xie, Y. Zhang, D. Xu, A. Manivannan, Z. Liu, Catalyst-free growth of three-dimensional graphene flakes and graphene/g-C<sub>3</sub>N<sub>4</sub> composite for hydrocarbon oxidation, *ACS Nano* 10 (2016) 3665–3673, <https://doi.org/10.1021/acsnano.6b00113>.

[33] L. Ma, H. Fan, K. Fu, S. Lei, Q. Hu, H. Huang, G. He, Protonation of graphitic carbon nitride (g-C<sub>3</sub>N<sub>4</sub>) for an electrostatically self-assembling Carbon@g-C<sub>3</sub>N<sub>4</sub> core–Shell nanostructure toward high hydrogen evolution, *ACS Sustain. Chem. Eng.* 5 (2017) 7093–7103, <https://doi.org/10.1021/acssuschemeng.7b01312>.

[34] J. Wang, D. Hao, J. Ye, N. Umezawa, Determination of crystal structure of graphitic carbon nitride: ab initio evolutionary search and experimental validation, *Chem. Mater.* 29 (2017) 2694–2707, <https://doi.org/10.1021/acs.chemmater.6b02969>.

[35] N.A. Mohamed, H. Ullah, J. Safaei, A.F. Ismail, M.F. Mohamad Noh, M.F. Soh, M.A. Ibrahim, N.A. Ludin, M.A. Mat Teridi, Efficient photoelectrochemical performance of  $\gamma$  irradiated g-C<sub>3</sub>N<sub>4</sub> and its g-C<sub>3</sub>N<sub>4</sub> @BiVO<sub>4</sub> heterojunction for solar water splitting, *J. Phys. Chem. C* 123 (2019) 9013–9026, <https://doi.org/10.1021/acs.jpcc.9b00217>.

[36] H. Ullah, A.A. Tahir, S. Bibi, T.K. Mallick, S.Zh. Karazhanov, Electronic properties of  $\beta$ -TaON and its surfaces for solar water splitting, *Appl. Catal. B* 229 (2018) 24–31, <https://doi.org/10.1016/j.apcatb.2018.02.001>.

[37] J. Safaei, H. Ullah, N.A. Mohamed, M.F. Mohamad Noh, M.F. Soh, A.A. Tahir, N. Ahmad Ludin, M.A. Ibrahim, W.N.R. Wan Isahak, M.A. Mat Teridi, Enhanced photoelectrochemical performance of Z-scheme g-C3N4/BiVO<sub>4</sub> photocatalyst, *Appl. Catal. B* 234 (2018) 296–310, <https://doi.org/10.1016/j.apcatb.2018.04.056>.

[38] H. Ullah, Inter-molecular interaction in Polypyrrole/TiO<sub>2</sub> 2 : a DFT study, *J. Alloys. Compd.* 692 (2017) 140–148, <https://doi.org/10.1016/j.jallcom.2016.08.169>.

[39] S.N.F.M. Nasir, H. Ullah, M. Ebadi, A.A. Tahir, J.S. Sagu, M.A. Mat Teridi, new insights into Se/BiVO<sub>4</sub> heterostructure for photoelectrochemical water splitting: a combined experimental and DFT study, *J. Phys. Chem. C* 121 (2017) 6218–6228, <https://doi.org/10.1021/acs.jpcc.7b01149>.

[40] H. Ullah, A.A. Tahir, T.K. Mallick, Polypyrrole/TiO<sub>2</sub> composites for the application of photocatalysis, *Sens. Actuators B Chem.* 241 (2017) 1161–1169, <https://doi.org/10.1016/j.snb.2016.10.019>.

[41] H. Ullah, A.A. Tahir, T.K. Mallick, Structural and electronic properties of oxygen defective and Se-doped p-type BiVO<sub>4</sub>(001) thin film for the applications of photocatalysis, *Appl. Catal. B* 224 (2018) 895–903, <https://doi.org/10.1016/j.apcatb.2017.11.034>.

[42] A. Du, S. Sanvito, Z. Li, D. Wang, Y. Jiao, T. Liao, Q. Sun, Y.H. Ng, Z. Zhu, R. Amal, S.C. Smith, Hybrid graphene and graphitic carbon nitride nanocomposite: gap opening, Electron–hole puddle, interfacial charge transfer, and enhanced visible light response, *J. Am. Chem. Soc.* 134 (2012) 4393–4397, <https://doi.org/10.1021/ja211637p>.

[43] F. Guinea, T. Low, Band structure and gaps of triangular graphene superlattices, *Philos. Trans. R. Soc. Lond. A: Math. Phys. Eng. Sci.* 368 (2010) 5391–5402, <https://doi.org/10.1098/rsta.2010.0214>.

[44] A. Du, S. Sanvito, Z. Li, D. Wang, Y. Jiao, T. Liao, Q. Sun, Y.H. Ng, Z. Zhu, R. Amal, S.C. Smith, Hybrid graphene and graphitic carbon nitride nanocomposite: gap opening, electron–hole puddle, interfacial charge transfer, and enhanced visible light response, *J. Am. Chem. Soc.* 134 (2012) 4393–4397, <https://doi.org/10.1021/ja211637p>.

[45] W.-D. Oh, L.-W. Lok, A. Veksha, A. Giannis, T.-T. Lim, Enhanced photocatalytic degradation of bisphenol A with Ag-decorated S-doped g-C3N4 under solar irradiation: performance and mechanistic studies, *Chem. Eng. J.* 333 (2018) 739–749, <https://doi.org/10.1016/j.cej.2017.09.182>.

[46] L. Jiang, X. Yuan, G. Zeng, J. Liang, Z. Wu, H. Yu, D. Mo, H. Wang, Z. Xiao, C. Zhou, Nitrogen self-doped g-C3N4 nanosheets with tunable band structures for enhanced photocatalytic tetracycline degradation, *J. Colloid Interface Sci.* 536 (2019) 17–29, <https://doi.org/10.1016/j.jcis.2018.10.033>.

[47] W. Guo, J. Zhang, G. Li, C. Xu, Enhanced photocatalytic activity of P-type (K, Fe) co-doped g-C3N4 synthesized in self-generated NH<sub>3</sub> atmosphere, *Appl. Surf. Sci.* 470 (2019) 99–106, <https://doi.org/10.1016/j.apsusc.2018.10.234>.

[48] E.S. Da Silva, N.M.M. Moura, A. Coutinho, G. Dražić, B.M.S. Teixeira, N.A. Sobolev, C.G. Silva, M.G.P.M.S. Neves, M. Prieto, J.L. Faria,  $\beta$ -Cyclodextrin as a precursor to holey C-doped g-C<sub>3</sub>N<sub>4</sub> nanosheets for photocatalytic hydrogen generation, *ChemSusChem* 11 (2018) 2681–2694, <https://doi.org/10.1002/cssc.201801003>.

[49] M. Humayun, Q. Fu, Z. Zheng, H. Li, W. Luo, Improved visible-light catalytic activities of novel Au/P-doped g-C3N4 photocatalyst for solar fuel production and mechanism, *Appl. Catal. A Gen.* 568 (2018) 139–147, <https://doi.org/10.1016/j.apcata.2018.10.007>.

[50] C. Liu, H. Huang, W. Cui, F. Dong, Y. Zhang, Band structure engineering and efficient charge transport in oxygen substituted g-C3N4 for superior photocatalytic hydrogen evolution, *Appl. Catal. B* 230 (2018) 115–124, <https://doi.org/10.1016/j.apcatb.2018.02.038>.

[51] S. Zhang, Y. Liu, P. Gu, R. Ma, T. Wen, G. Zhao, L. Li, Y. Ai, C. Hu, X. Wang, Enhanced photodegradation of toxic organic pollutants using dual-oxygen-doped porous g-C3N4: mechanism exploration from both experimental and DFT studies, *Appl. Catal. B* 248 (2019) 1–10, <https://doi.org/10.1016/j.apcatb.2019.02.008>.

[52] X. Yang, L. Tian, X. Zhao, H. Tang, Q. Liu, G. Li, Interfacial optimization of g-C3N4-based Z-scheme heterojunction toward synergistic enhancement of solar-driven photocatalytic oxygen evolution, *Appl. Catal. B* 244 (2019) 240–249, <https://doi.org/10.1016/j.apcatb.2018.11.056>.

[53] Y. Yu, J. Geng, H. Li, R. Bao, H. Chen, W. Wang, J. Xia, W.-Y. Wong, Exceedingly high photocatalytic activity of g-C<sub>3</sub>N<sub>4</sub>/Gd<sub>2</sub>N-TiO<sub>2</sub> composite with nanoscale heterojunctions, *Sol. Energy Mater. Sol. Cells* 168 (2017) 91–99, <https://doi.org/10.1016/j.solmat.2017.04.023>.

[54] M. Karimi-Nazarabad, E.K. Goharshadi, Highly efficient photocatalytic and photoelectrocatalytic activity of solar light driven WO<sub>3</sub>/g-C3N4 nanocomposite, *Sol. Energy Mater. Sol. Cells* 160 (2017) 484–493, <https://doi.org/10.1016/j.solmat.2016.11.005>.